INTERNATIONAL JOURNAL FOR NUMERICAL METHODS IN FLUIDS, VOL. 14, 729–751 (1992)

A LEAST-SQUARES METHOD FOR SOLVING THE MIXED FORM OF THE GROUNDWATER FLOW EQUATIONS

L. R. BENTLEY AND G. F. PINDER

College of Engineering and Mathematics, University of Vermont, Burlington, Vt 05405, U.S.A.

SUMMARY

The mixed form of the areal groundwater flow equations is solved with a least-squares finite element procedure (LESFEM). Hydraulic head and x- and y-directed fluxes are state variables. Physical parameters and state variables are approximated using a bilinear basis. Grid refinements and irregular domain boundaries are implemented on rectangular meshes.

Residuals are constructed at collocation points for conservation of mass and Darcy's law. Boundary condition residuals are constructed at discrete points along the boundary. The residuals are weighted, squared and summed. A set of algebraic equations is formed by taking the derivatives of the weighted sum of the squares of the residuals with respect to each unknown parameter in the approximation for the state variable and setting them to zero.

Proper choice of a potential scaling parameter and residual weights is essential for the effective application of the algorithm. Test problem results demonstrate that the method is effective for both transient and steady state cases.

The LESFEM algorithm generates a C^0-continuous velocity field. The continuous velocity field and the rectangular mesh simplify the implementation of algorithms that require tracking. In addition, rectangular *meshes simplify* mesh and boundary generation.

KEYWORDS Least squares Mixed formulation Collocation Groundwater Vertically averaged flow

INTRODUCTION

Eulerian–Lagrangian procedures for solving the transport equation require an accurate velocity field to accommodate the tracking step. In general, the velocity field must be generated by numerically solving the partial differential equations that govern flow. This paper introduces a numerical procedure for solving the mixed form of the vertically averaged groundwater flow equations. The algorithm (LESFEM) is based on a least-squares finite element procedure.

Perhaps the most popular method used to solve groundwater flow problems is the Galerkin finite element method. The method is popular because irregular domain boundaries can be represented and boundary conditions are easily incorporated into the governing equation. The method, as normally applied, employs non-rectangular elements. Such elements complicate tracking procedures. In addition, typical Galerkin-based algorithms produce velocity fields that are piecewise-constant or C^{-1}-continuous. Also, mesh generation is often labour-intensive and cumbersome.

Least-squares procedures have been applied to parabolic partial differential equations,[1–3] but few researchers have applied them directly to groundwater flow problems.[4] Using least squares,

0271–2091/92/060729–23$11.50

Received 29 January 1991
Revised 29 May 1991

irregular domains can be defined on rectangular meshes[4,5] and a grid refinement strategy can be developed that uses rectangular elements. Consequently, the generation of element connectivities and nodal locations is easily automated. Similarly, the boundary geometry can be easily generated from a set of co-ordinates which define straight line segments that approximate the boundary. Any type of boundary condition can be accommodated using a penalty method. Finally, use of an orthogonal mesh simplifies tracking.

Groundwater flow is commonly simulated by using hydraulic head as the state variable and solving a partial differential equation of second order in space. The resulting head distribution is subsequently differentiated and substituted into Darcy's law to generate flux values. The solution of this form of the equation with a least-squares method requires a C^1-continuous basis, leading to serious difficulties. However, a lower-order continuity basis can be used by solving an equivalent system of coupled first-order partial differential equations.[1,6-8] In addition, pathologic behaviour in the head field tends to be amplified when the fluxes are computed, because the heads are differentiated during the application of Darcy's law. The differentiation of heads to generate fluxes also lowers the order of the spatial approximation of the fluxes relative to that of the heads. Researchers have reduced the pathologies in the fluxes and raised the relative order of approximation of the fluxes by using the mixed form of the flow equations.[9,10] The mixed form of the flow equations is a coupled set of first-order partial differential equations wherein the two directions of flux, as well as the hydraulic head, are considered as state variables.

In order to improve the relative accuracy of the velocity field and to reduce the basis continuity requirements, the mixed form of the groundwater flow equations is used in the following development. Use of the mixed formulation leads to C^0-continuous fluxes. Combining the fluxes with a C^0-continuous parameter field yields a C^0-continuous velocity field. As mentioned earlier, continuous velocities are desirable for tracking in the application of Eulerian–Lagrangian methods.

VERTICALLY AVERAGED FLOW EQUATIONS

For the reasons outlined in the Introduction, areal ground water flow will be described by the following system of three coupled equations: the vertically averaged conservation of mass, the vertically averaged Darcy's law in the x-direction and the vertically averaged Darcy's law in the y-direction. Three variables will be used to describe the state of the system: the vertically averaged hydraulic head h, the vertically averaged flux in the x-direction, q_x, and the vertically averaged flux in the y-direction, q_y.

The vertically averaged forms of the conservation-of-mass equation and Darcy's law can be found, for example, in Reference 11. The conservation-of-mass equation is

$$S\frac{\partial h}{\partial t}+\frac{\partial q_x}{\partial x}+\frac{\partial q_y}{\partial y}+B(h-h_r)-I-Q_p\delta(\mathbf{x}-\mathbf{x}_p)=0, \quad \mathbf{x}\in\Omega, \tag{1}$$

where S is the storage coefficient, x and y are spatial co-ordinates, $\mathbf{x}$ is a spatial co-ordinate vector, t is time, B is leakance, h_r is a leakage reference head, I is infiltration and Ω is the domain of the aquifer which is bounded by $\delta\Omega$. The source term Q_p represents point sinks and sources such as pumping or injection wells, while $\delta(\mathbf{x}-\mathbf{x}_p)$ is the Dirac delta function. All fluxes are positive into the domain Ω. Darcy's law in the x-direction is

$$q_x+T_{xx}\frac{\partial h}{\partial x}+T_{xy}\frac{\partial h}{\partial y}=0, \quad \mathbf{x}\in\Omega, \tag{2}$$

and Darcy's law in the y-direction is

$$q_y + T_{yx}\frac{\partial h}{\partial x} + T_{yy}\frac{\partial h}{\partial y} = 0, \quad \mathbf{x} \in \Omega, \tag{3}$$

where T_{ij} are elements of the transmissivity tensor. Transmissivity tensor elements are equal to the hydraulic conductivity tensor elements K_{ij} times the layer thickness l.

When the aquifer is confined, the equations are linear. When the aquifer is unconfined, the saturated layer thickness $l \equiv h - b$ is a function of the head and the aquifer bottom elevation b. Since the transmissivity $T_{ij} \equiv lK_{ij}$ is dependent on the hydraulic head, equations (2) and (3) become non-linear. The specific yield S_y and the specific storage S_s are related to the storage coefficient by $S = S_y + lS_s$. Because the storage coefficient is dependent on h, equation (1) is also non-linear for an unconfined aquifer. However, this equation is only weakly non-linear, because the specific yield tends to be much larger than the specific storage.

The initial state of h, q_x and q_y must be specified and their values are denoted as $\bar{h}_0$, $\bar{q}_{x0}$ and $\bar{q}_{y0}$ respectively. Boundary conditions may be of three types: specified head,

$$h - \bar{b}_1 = 0, \quad \mathbf{x} \in \delta\Omega_1, \tag{4a}$$

specified flux,

$$\mathbf{q}\cdot\mathbf{n} - \bar{b}_2 = (q_x \cos v + q_y \sin v) - \bar{b}_2 = 0, \quad \mathbf{x} \in \delta\Omega_2, \tag{4b}$$

and mixed conditions,

$$-B_b(h - h_{br}) + \mathbf{q}\cdot\mathbf{n} = -B_b(h - h_{br}) + (q_x \cos v + q_y \sin v) = 0, \quad \mathbf{x} \in \delta\Omega_3, \tag{4c}$$

where $\delta\Omega_i$ is the segment of boundary associated with the ith-type boundary condition, $\bar{b}_i$ are the specified boundary values, $\mathbf{q}$ is the flux vector, $\mathbf{n}$ is the outward-directed normal vector, v is the angle of the outward-directed normal measured counterclockwise from the positive x-direction and B_b and h_{br} are boundary leakage parameters.

SPATIAL DISCRETIZATION

Grid definition follows the general approach of Laible and Pinder.[5] In this approach, grid refinements and irregular domain boundaries are superimposed on orthogonal meshes. Grid definition begins with a rectangular mesh oriented along the x- and y-axes as illustrated in Figure 1. The elements in this coarse mesh are called grid blocks. The size of the grid blocks should be the dimension of the largest element in any row or column of the final grid. The example in Figure 1 has a pattern of 10 grid blocks by 10 grid blocks.

Grid blocks can be refined by divisions of integral powers of two. For example, a grid refinement of two means that each side of the grid block is split in the centre and four elements are created. The example in Figure 1 has 12 grid blocks refined by two and four grid blocks refined by four. When two grid blocks of different refinement share a side, 'hanging nodes' are created. Node 2 in Figure 1 is an example of a hanging node. The hanging nodes have associated trial functions which are active on only one side of the element boundary and, as will be detailed later, they will require special treatment. Grid blocks which share a common side are allowed to vary by a maximum of one refinement level. This requirement assures that aberrations due to vastly different adjacent refinements do not arise.

The domain boundary is projected onto the final mesh by specifying the co-ordinates of the intersections of the element boundaries with the domain boundary (see Figure 2). The domain

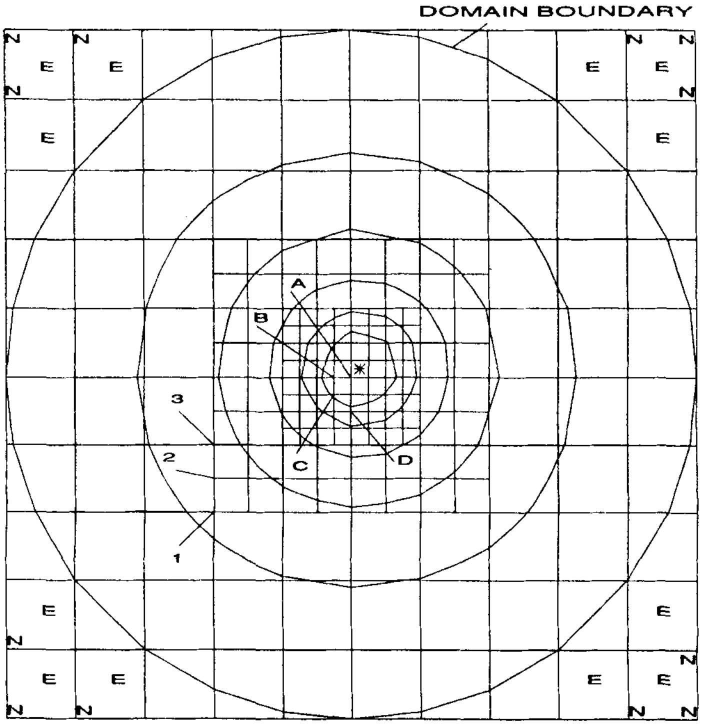

Figure 1. Pumping well in a circular aquifer. A circular aquifer of radius 1000 m is discretized with an orthogonal mesh. The co-ordinate origin is located at the centre of the aquifer (node A). The largest elements are 200 m x 200 m and the most refined elements are 50 m x 50 m. The star indicates a pumping well located at (25 m, 25 m). Steady state hydraulic heads are contoured at the interval of 0·05 m, with the zero contour falling on the circular domain boundary. Nodes labelled N and elements labelled E are inactive

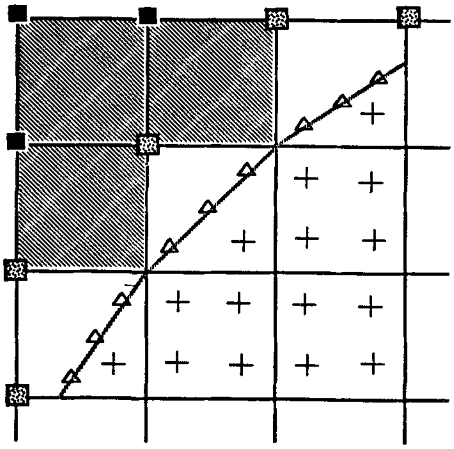

Figure 2. Irregular domain boundary. The rectangular mesh (solid lines) is cut by an irregular domain boundary (broken line) which is enforced with penalty points (triangles). Inactive elements are cross-hatched and inactive nodes are represented by solid squares. Only collocation points which fall within the domain (pluses) are used in the sum of the squared residuals. Speckled squares are active nodes located outside the boundary

boundary is assumed to lie along straight lines connecting the intersections. Figure 1 demonstrates a circular boundary that has been approximated by a series of straight line segments.

After the boundary has been projected onto the mesh, some elements may lie completely outside the domain and they are eliminated from the problem (see Figure 2). Nodes which are connected only to inactive elements are also eliminated. The example presented in Figure 1 contains 12 inactive nodes labelled N and 12 inactive elements labelled E.

Each of the three state variables is approximated with bilinear trial functions on the previously described rectangular grid. Following standard finite element protocol, a local co-ordinate system is defined,

$$\xi=\frac{2(x-x^e)}{\Delta x^e}-1, \tag{5a}$$

$$\eta=\frac{2(y-y^e)}{\Delta y^e}-1, \tag{5b}$$

where x^e and y^e are the co-ordinates of the lower left corner of the eth element and Δx^e and Δy^e are the element side dimensions.

In the local co-ordinate system the four basis functions within an element can be written

$$\psi_i(\xi,\eta)=\tfrac{1}{4}(1+\xi\xi_i)(1+\eta\eta_i), \quad i=1,\ldots,4, \tag{6}$$

where ξ_i and η_i are the local co-ordinates of the ith node and take on values of positive and negative unity. A cardinal basis function $\Psi_J(x, y)$ can be constructed for the Jth node by combining the appropriate bilinear basis functions from elements that are connected to the node. Although the cardinal basis functions are never constructed, they are used to define the trial functions

$$\hat{h}=\sum_{J=1}^{M} H_J(t)\Psi_J(x,y), \tag{7a}$$

$$\hat{q}_x=\sum_{J=1}^{M} QX_J(t)\Psi_J(x,y), \tag{7b}$$

$$\hat{q}_y=\sum_{J=1}^{M} QY_J(t)\Psi_J(x,y), \tag{7c}$$

where M equals the number of active nodes and $H_J(t)$, $QX_J(t)$ and $QY_J(t)$ are the time-varying values of the state variables at the Jth node.

Anticipating the form of the least-squares equations, $\hat{h}$ must be at least C^0-continuous, $\hat{q}_x$ must be at least C^0-continuous in x and piecewise-continuous in y and $\hat{q}_y$ must be at least C^0-continuous in y and piecewise-continuous in x. The continuity of the trial spaces is maintained by setting the values of the state variables at the hanging nodes to the average values of the state variables at the two adjacent nodes along the element boundary line containing the hanging node. For example,

$$H_2(t)=\frac{H_1(t)+H_3(t)}{2}. \tag{8}$$

Although only one of the fluxes must be continuous at a hanging node, both fluxes are slaved at hanging nodes in order to maintain a fully continuous flux field.

Good results have been obtained by defining parameters constant over elements, but the velocity fields that are generated are not necessarily continuous. Consequently, parameters are specified at all nodes except hanging nodes. The values at hanging nodes are set to the average of the values of the two nodes bracketing the hanging node, in the same manner as demonstrated in equation (8) for head. Interior to elements, the parameter values are interpolated using the bilinear basis of equation (6). Thus all parameters are C^0-continuous. Since fluxes are C^0-continuous, the resulting velocity field will also be C^0-continuous. The parameters that must be assigned to each node are horizontal hydraulic conductivity K_{xx}, K_{yy} and $K_{xy}=K_{yx}$, specific storage S_s, leakance B, leakage reference head h_r and infiltration rate I. Further, if the aquifer is confined, the layer thickness l must be specified. If the aquifer is unconfined, the specific yield S_y and the elemental bottom elevation b are specified.

LEAST SQUARES EQUATIONS

Errors or residuals arise whenever the trial functions do not exactly meet conditions which arise from the mathematical description of the physical system. In the LESFEM method, individual collocation point errors are squared, multiplied by a weight and then summed to form the weighted sum of the squares of the errors, which herein is denoted ε. The sum of the squares of the errors is minimized by taking the derivatives of the sum of squares with respect to each of the unknown degrees of freedom appearing in the approximations of the state variables, equations (7), and setting the results to zero.

At this point it is convenient to introduce a potential scaling parameter P such that scaled head $H'_J=H_J/P$. The parameter P is used to adjust the magnitudes of the state variables so that fluxes and heads are roughly equivalent. The choice of the value of P is discussed later.

A conservation-of-mass residual is formed by substituting the trial functions, equations (7), into the conservation-of-mass equation (1) and evaluating the result at a point $\mathbf{x}_k$:

$$Rm_k=\sum_{J=1}^{N}\left(PS^k\Psi_J^k\frac{\mathrm{d}H'_J}{\mathrm{d}t}+QX_J\frac{\partial\Psi_J^k}{\partial x}+QY_J\frac{\partial\Psi_J^k}{\partial y}+B^kPH'_J\Psi_J^k\right)-B^kh_r^k-I^k-Q_p\delta(\mathbf{x}_k-\mathbf{x}_p), \tag{9}$$

where superscript k indicates evaluation at the point $\mathbf{x}_k$. The time derivative in equation (9) is approximated by an implicit finite difference and the equation is transformed to the local co-ordinate system. After some rearranging, a conservation-of-mass residual becomes

$$\begin{aligned}Rm_k=\sum_{j^e=1}^{4}&\left(P\left(\frac{S^k}{\Delta t}+B^k\right)\psi_{j^e}^kH'_{j^e}+\frac{2}{\Delta x^e}\frac{\partial\psi_{j^e}^k}{\partial\xi}QX_{j^e}+\frac{2}{\Delta y^e}\frac{\partial\psi_{j^e}^k}{\partial\eta}QY_{j^e}\right)\\&-\left(\frac{PS^k}{\Delta t}\hat{h}_k^{n-1}+B^kh_r^k+I^k+Q_p\delta(\mathbf{x}_k-\mathbf{x}_p)\right),\end{aligned} \tag{10}$$

where the coefficients H'_{j^e}, QX_{j^e} and QY_{j^e} are the nodal values of the trial functions of the scaled head and the fluxes at the solution time level n respectively, $\hat{h}_k^{n-1}$ is the value of the trial function at location $\mathbf{x}_k$ and the previous time level $n-1$ and j^e are the node indices of the four nodes attached to element e. Whenever j^e is a hanging node, the average of the two adjacent nodes is used as indicated in equation (8).

The Darcy's law residuals are formed by substituting the trial functions, equations (7), into the Darcy's law equations (2) and (3) and evaluating the resulting expression at the collocation point locations $\mathbf{x}_k$:

$$Rq_{x,k}=\sum_{j^e=1}^{4}\psi_{j^e}^kQX_{j^e}+\left(PT_{xx}^k\frac{2}{\Delta x^e}\frac{\partial\psi_{j^e}^k}{\partial\xi}+PT_{xy}^k\frac{2}{\Delta y^e}\frac{\partial\psi_{j^e}^k}{\partial\eta}\right)H'_{j^e}, \tag{11}$$

$$Rq_{y,k}=\sum_{j^e=1}^{4}\psi_{j^e}^k\,QY_{j^e}+\left(PT_{yx}^k\frac{2}{\Delta x^e}\frac{\partial\psi_{j^e}^k}{\partial\xi}+PT_{yy}^k\frac{2}{\Delta y^e}\frac{\partial\psi_{j^e}^k}{\partial\eta}\right)H'_{j^e}. \tag{12}$$

Residuals for the first-, second- and third-type boundary conditions are formed by substituting the trial functions, equations (7), into the boundary condition equations (4) and evaluating the results at the collocation points l_1, l_2 and l_3 respectively:

$$Rb_{1,l_1}=\sum_{j^e=1}^{4}\psi_{j^e}^{l_1}H'_{j^e}-\frac{\bar{b}_1^{l_1}}{P}, \tag{13a}$$

$$Rb_{2,l_2}=\sum_{j^e=1}^{4}(\psi_{j^e}^{l_2}\cos v^{l_2}QX_{j^e}+\psi_{j^e}^{l_2}\sin v^{l_2}QY_{j^e})-\bar{b}_2^{l_2}, \tag{13b}$$

$$Rb_{3,l_3}=\sum_{j^e=1}^{4}(PBb^{l_3}\psi_{j^e}^{l_3}H'_{j^e}+\psi_{j^e}^{l_3}\cos v^{l_3}QX_{j^e}+\psi_{j^e}^{l_3}\sin v^{l_3}QY_{j^e})-B_{\mathrm{b}}^{l_3}h_{\mathrm{br}}^{l_3}. \tag{13c}$$

The weighted sum of the squares of the residuals is

$$\varepsilon=\sum_{k=1}^{NK}(Wm_k^2Rm_k^2+Wq_{x,k}^2Rq_{x,k}^2+Wq_{y,k}^2Rq_{y,k}^2)+\sum_{l_1=1}^{NB_1}Wb_{1,l_1}^2Rb_{1,l_1}^2+\sum_{l_2=1}^{NB_2}Wb_{2,l_2}^2Rb_{2,l_2}^2$$
$$+\sum_{l_3=1}^{NB_3}Wb_{3,l_3}^2Rb_{3,l_3}^2, \tag{14}$$

where the Ws are weights associated with a residual type and collocation point location and NK, NB_1, NB_2 and NB_3 are the total numbers of the various types of collocation points. Collocation point weight selection is discussed later.

If there are M active nodes in the mesh, equation (14) contains $3M$ unknowns. A system of $3M$ equations is generated by taking the derivative of equation (14) with respect to each of the unknowns and setting it to zero. Examination of equations (10)–(13) reveals that some residuals do not contain all of the state variable types and some of the residual derivatives will be identically equal to zero. After eliminating the zero terms, the least-squares system of equations becomes:

$$\sum_{k=1}^{NK}\left(Wm_k^2Rm_k\frac{\partial Rm_k}{\partial H'_I}+Wq_{x,k}^2Rq_{x,k}\frac{\partial Rq_{x,k}}{\partial H'_I}+Wq_{y,k}^2Rq_{y,k}\frac{\partial Rq_{y,k}}{\partial H'_I}\right)$$
$$+\sum_{l_1=1}^{NB_1}Wb_{1,l_1}^2Rb_{1,l_1}\frac{\partial Rb_{1,l_1}}{\partial H'_I}+\sum_{l_3=1}^{NB_3}Wb_{3,l_3}^2Rb_{3,l_3}\frac{\partial Rb_{3,l_3}}{\partial H'_I}=0,\qquad I=1,\ldots,M, \tag{15a}$$

$$\sum_{k=1}^{NK}\left(Wm_k^2Rm_k\frac{\partial Rm_k}{\partial QX_I}+Wq_{x,k}^2Rq_{x,k}\frac{\partial Rq_{x,k}}{\partial QX_I}\right)$$
$$+\sum_{l_2=1}^{NB_2}Wb_{2,l_2}^2Rb_{2,l_2}\frac{\partial Rb_{2,l_2}}{\partial QX_I}+\sum_{l_3=1}^{NB_3}Wb_{3,l_3}^2Rb_{3,l_3}\frac{\partial Rb_{3,l_3}}{\partial QX_I}=0,\qquad I=1,\ldots,M, \tag{15b}$$

$$\sum_{k=1}^{NK}\left(Wm_k^2Rm_k\frac{\partial Rm_k}{\partial QY_I}+Wq_{y,k}^2Rq_{y,k}\frac{\partial Rq_{y,k}}{\partial QY_I}\right)$$
$$+\sum_{l_2=1}^{NB_2}Wb_{2,l_2}^2\frac{\partial Rb_{2,l_2}}{\partial QY_I}+\sum_{l_3=1}^{NB_3}Wb_{3,l_3}^2Rb_{3,l_3}\frac{\partial Rb_{3,l_3}}{\partial QY_I}=0,\qquad I=1,\ldots,M. \tag{15c}$$

Equation (15) represent the set of discrete equations that must be solved in the least-squares groundwater flow problem. The equations form symmetric, positive definite system matrices. The element entries for the system matrix and right-hand-side vectors are detailed in the Appendix.

When the aquifer is unconfined, the flow equations are non-linear and are solved by Jacobi iteration.

COLLOCATION POINT LOCATIONS

In most numerical methods, locating collocation or integration points at the Gauss points will yield the most accurate solutions, and convergence studies show that LESFEM is not an exception. The use of more than four collocation points per element may in some cases marginally improve the solution, but the improvements are generally not worth the increased computational effort. Consequently, as shown in Figure 2, four interior collocation points are located at the Gauss points of each element. If the element is a boundary element and the Gauss point is outside the domain boundary, the point is not used. Three boundary collocation points per boundary element are equally spaced along the straight line segment that passes through the boundary element.

POINT SOURCES

Equation (10) is singular at locations $\mathbf{x}_p$ due to the point sources. In order to avoid the difficulties surrounding the evaluation of residuals at singular points, point sources are approximated by source elements. Within source elements, $Q_p\delta(\mathbf{x}_k-\mathbf{x}_p)$ is replaced by an areal source term of strength $Q_p/\Delta x^e \Delta y^e$.

The flux trial functions are not capable of matching the solution in the immediate *vicinity of the* source. Whether the source is located at a node or within an element, the bilinear trial functions associated with the fluxes must pass through zero as they go from positive to negative through the source location. In reality, the flux goes to large-magnitude positive and negative values depending on the direction from which the source is approached. Consequently, the magnitude of the flux is severely underpredicted by the trial function near the source. The Darcy's law residuals relate the magnitude of the fluxes to the magnitude of the gradient of the heads, and the large flux errors cause the gradient of the head to be underpredicted. Although the flux may be well represented at the nodes surrounding the source, the heads are contaminated by the large local flux errors, causing errors to propagate into the rest of the domain.

A special procedure is required in order to avoid the problems just described. Point sources are located within elements. Realizng that Darcy's law will cause the heads to be contaminated by the large local flux errors associated with source elements, the Darcy's law equations are 'turned off' inside source elements. When a source element is identified, all the contributions associated with Darcy's law are eliminated by setting the $Wq_{x,k}$ and $Wq_{y,k}$ to zero in the source elements.

As the examples will demonstrate, the above-described procedure performs well. However, the purpose of the flow code is to generate tracking velocities, and the flux within the source element is poorly predicted. In order to avoid tracking difficulties near point sources, a local interpolating function is added to the trial function after the solution has been computed. The form of the additional term is derived from the steady state Thiem[12] solution of a well in an infinite aquifer:

$$q_{xs,p}=\frac{Q_p}{2\pi}\frac{x-x_p}{r_p^2}\left(1-\frac{r_p}{R_p}\right), \quad r_p<R_p, \tag{16a}$$

$$q_{xs,p}=0 \quad r_p>R_p, \tag{16b}$$

$$q_{ys,p}=\frac{Q_p}{2\pi}\frac{y-y_p}{r_p^2}\left(1-\frac{r_p}{R_p}\right), \quad r_p<R_p, \tag{16c}$$

$$q_{ys,p}=0, \quad r_p>R_p, \tag{16d}$$

where r_p is the distance to the pth well and R_p is set to assure that the influence of the interpolating functions is restricted to the source element. The source functions are simply added to the appropriate trial functions during the tracking step or when computing dispersion tensor values from dispersivities and velocity. Since the expressions are derived from a steady state solution, they will tend to overpredict fluxes in the source element during the earliest stages of transient solutions. It is emphasized that these expressions have no influence on the flow calculation. An example calculation with a pumping well is reported in a later section and the results will illustrate the relation between the singular flux function, the linear trial space and the analytical solution (see Figure 6).

WEIGHTS AND SCALING

The potential scaling parameter P is chosen so that the fluxes and the scaled heads are of equivalent magnitudes. If we define the parameters $\langle T_{xx} \rangle$ and $\langle T_{yy} \rangle$ as the representative values of the transmissivity tensor and $\langle \Delta x \rangle$ and $\langle \Delta y \rangle$ as the representative values of the grid elements, then

$$P = \frac{\langle \Delta x \rangle}{\langle T_{xx} \rangle} = \frac{\langle \Delta y \rangle}{\langle T_{yy} \rangle} \tag{17}$$

will balance the terms in equations (11) and (12). When the spatial discretization and the transmissivity values vary widely and create a large range of appropriate values of parameter P, it is best to choose one from the high side of the range. Note that this equation indicates that in selecting the aspect ratio of the grid one should take into account the anisotropy of the transmissivity tensor. However, anisotropy is typically not large for horizontal flow problems.

The interior weights are chosen to make the conservation-of-mass residuals, equation (10), and the two Darcy's law residuals, equations (11) and (12), of the order of unity in the terms involving the state variables:

$$Wm_k = \mathrm{MIN}\left(\Delta x^e, \Delta y^e, \frac{1}{P(S^k/\Delta t + B^k)}\right), \tag{18a}$$

$$Wq_{x,k} = \frac{\Delta x^e}{2PT^k_{xx}}, \tag{18b}$$

$$Wq_{y,k} = \frac{\Delta y^e}{2PT^k_{yy}}. \tag{18c}$$

Practical experience has shown that although these weights are often sufficient, global mass errors of the order of 5% can develop. In such cases the conservation-of-mass weights should be increased by a factor of two to three to improve the results.

When flow is steady, the flow equations become an elliptic system. If, in addition, the discretization interval is constant and the transmissivities are isotropic and homogeneous, then the weighting of equation (18) is consistent with the governing equation weights derived by Aziz *et al.*[8] for the least-squares solution of elliptic systems. In this case the weighting scheme causes the conservation-of-mass residual to be multiplied by the discretization interval, compensating for the difference in units between the conservation-of-mass equation and the Darcy's law equation.

Boundary weights should be chosen so that they are large enough to enforce the boundary conditions but not of unlimited magnitude. If the boundary weights are too large, then the conservation-of-mass and Darcy's law residuals become relatively small and will no longer sufficiently influence the solution. This can result in erratic behaviour of the flux and head values near the boundaries. If the boundary weights are too small, the boundary conditions will not be enforced, resulting in oscillatory or unstable solutions. Experience to date has been that solutions are relatively insensitive to boundary weights over several orders of magnitude. Only small variations between solutions have been observed while using weights of the order of 10–10^5, but use of the smaller values improves the conditioning of the system matrix.

The degrees of freedom associated with nodes outside the domain boundary but still connected to active elements may require special consideration. This is especially true when only a small part of the active element is within the domain boundary. To accommodate this situation, a very small value is added to the diagonal element of the system matrix of the equations associated with degrees of freedom located outside the domain. These weights, typically of the order of 10^{-8}, provide a slight bias to zero and control unwanted oscillations.

Generally, the more suitable the trial space is for representing the actual solution to the discrete equations, the less sensitive the computed solution is to the weighting. As a grid is refined, the sensitivity of the solution to the weights decreases. If solutions are very sensitive to weighting, it may indicate that the grid is insufficiently refined.

CONVERGENCE

The spatial convergence of the method was studied heuristically. A domain of length 1000 and one element width was divided into two, five, 10, 20 and 40 elements. Boundary conditions are $\hat{h}(x=0)=0$, $\hat{h}(x=1000)=10$ and $\hat{q}_y(y=0)=\hat{q}_y(y=\Delta Y)=0$. The simulated aquifer was confined and of unit thickness, with hydraulic conductivity $K_{xx}=K_{yy}=1+9x/1000$ and $K_{xy}=0$. Weighting and scaling were as follows: potential parameter $P=\Delta x$, boundary weights $Wb=10^3$ and mass conservation weights, equation (18a), were increased by a factor of two.

Using the analytical solution, the error in the LESFEM-computed heads and x-directed flux was computed at each of the nodes and each of the Gauss points. A plot of the logarithm of the maximum error in the heads versus the logarithm of the element length for the Gauss points and for the nodes is presented in Figure 3A. A similar plot for the x-directed flux is presented in Figure 3B. The results are consistent with first-order spatial convergence of both flux and head in the L_∞-norm.

A plot of the logarithm of the L_2-error of the LESFEM-computed heads versus the logarithm of the element length for the Gauss points and for the nodes is presented in Figure 4A and that for the x-directed flux in Figure 4B. These results indicate that LESFEM convergence rates in the L_2-norm are approaching second-order for both head and flux. These results compare favourably with the theoretical results of Aziz *et al.*[8]

PUMPING WELL IN A CIRCULAR AQUIFER

The following examples simulate a pumping well in a homogeneous confined circular aquifer of radius 1000 m. A pumping well of strength $10^{-3}\ \mathrm{m^3\,s^{-1}}$ is located near the centre of the aquifer at $x=25$ m, $y=25$ m. The boundary of the domain, the source location and the grid used for the simulation are illustrated in Figure 1. The aquifer has a uniform thickness of $l=10$ m. The hydraulic conductivity, $K_{xx}=K_{yy}=1{\cdot}4\times10^{-4}\ \mathrm{m\,s^{-1}}$ and $K_{xy}=0$, and the specific storage, $S_s=1{\cdot}5\times10^{-5}\ \mathrm{m^{-1}}$, values correspond to typical values for a medium-grained sand. A zero-hydraulic-head condition is applied along the straight line segments that approximate the circular boundary and the initial head is zero everywhere. For the transient results an initial time step of

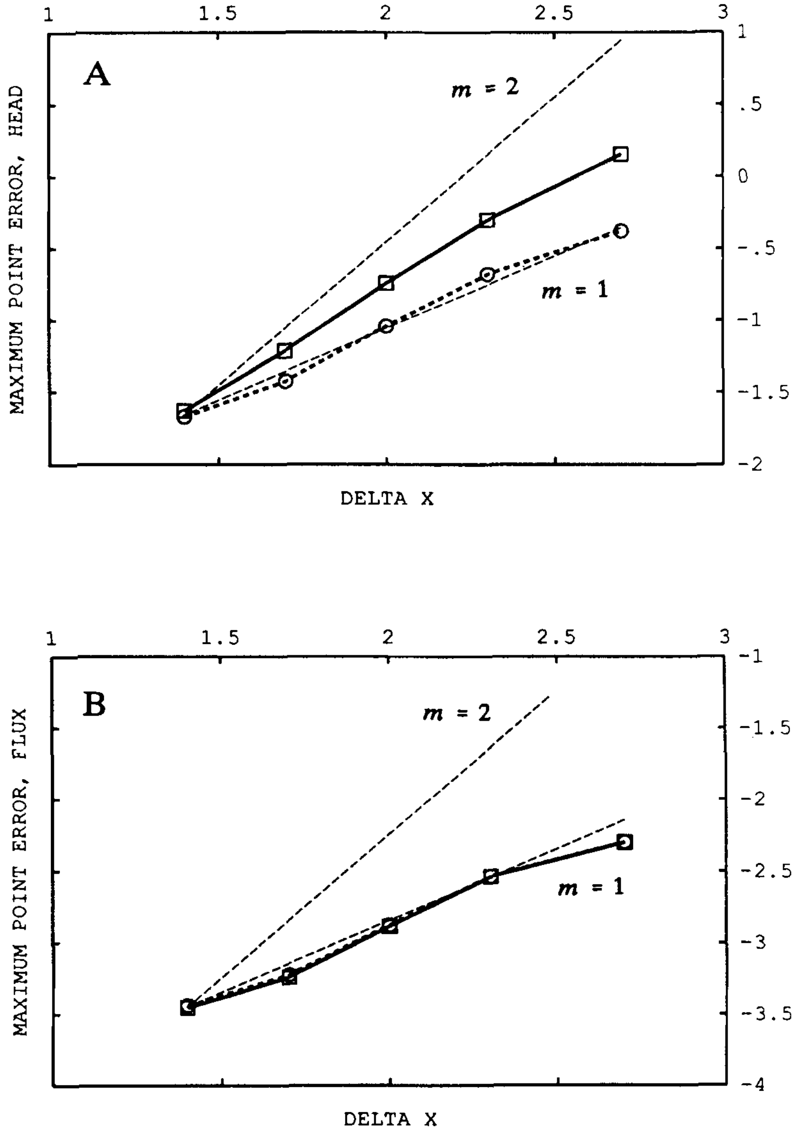

Figure 3. Convergence of maximum point errors. The logarithm of the maximum error at the Gauss points (squares) and the nodes (circles) is plotted versus the logarithm of the element length for (A) head and (B) x-directed flux. Dashed lines indicate first-order ($m = 1$) and second-order ($m = 2$) convergence

10 s was used. The time step was subsequently increased by a factor of 1·5 every five time steps. A total of 85 time steps were computed.

The potential scale is $P = 1{\cdot}4 \times 10^5$ and the interior residual weights were computed using equations (18). The first-type boundary is enforced with weight $Wb_{1,l_1} = 1{\cdot}0 \times 10^3$.

An analytical solution of the drawdown versus time for a pumping well in an infinite aquifer was derived by Theis.[12] The LESFEM drawdown results at four locations are compared with the Theis solutions in Figure 5. Near the source the LESFEM drawdowns show some departure

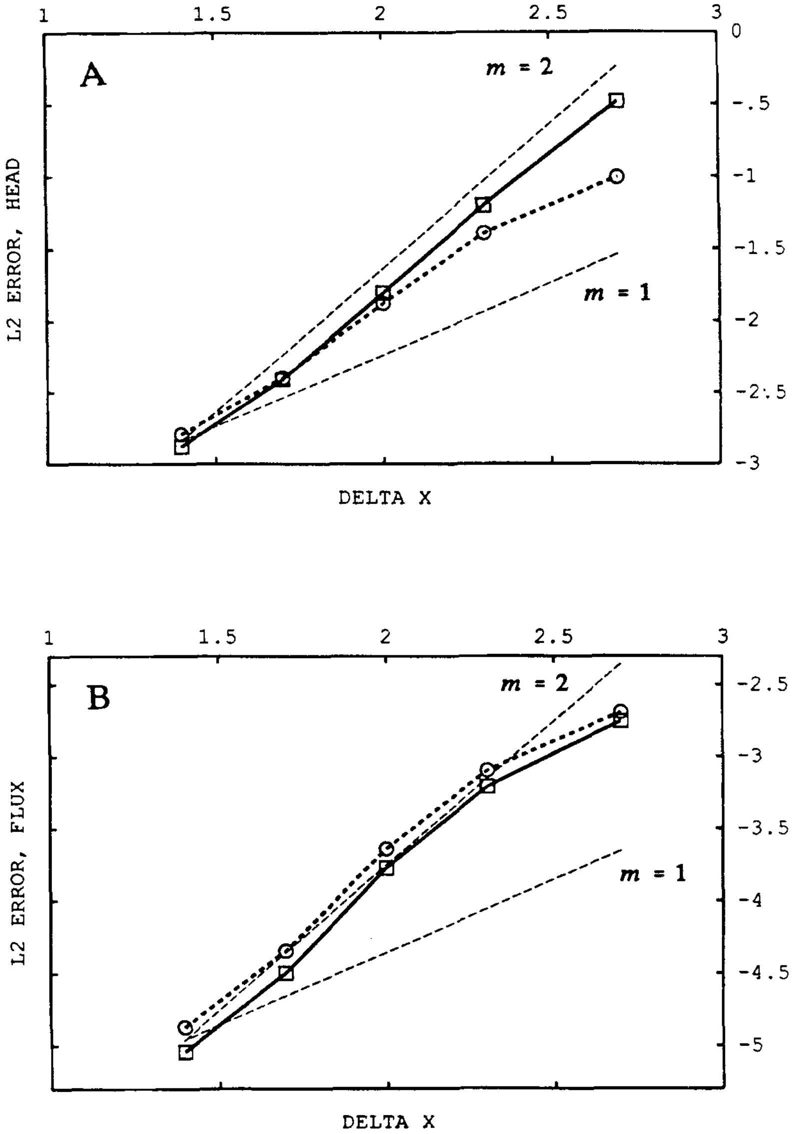

Figure 4. Convergence of L_2-errors. The logarithm of the average L_2-error at the Gauss points (squares) and the nodes (circles) is plotted versus the logarithm of the element length for (A) head and (B) x-directed flux. Dashed lines indicate first-order ($m = 1$) and second-order ($m = 2$) convergence

at early time, but, as time progresses, the solutions match well in all regions. Finally, as the constant-head boundary begins to influence the computed solution, the LESFEM heads stop decreasing and the computed solution approaches steady state.

Eventually, the transient solution to this problem reaches steady state. Alternatively, the steady state result can be computed in one step by setting the storage term to zero. The steady state heads of the one-step solution are contoured in Figure 1. The zero-head contour falls directly on the imposed zero-head boundary and the contour interval is 0·05 m. Contours are circular and centred on the slightly non-symmetric location of the source.

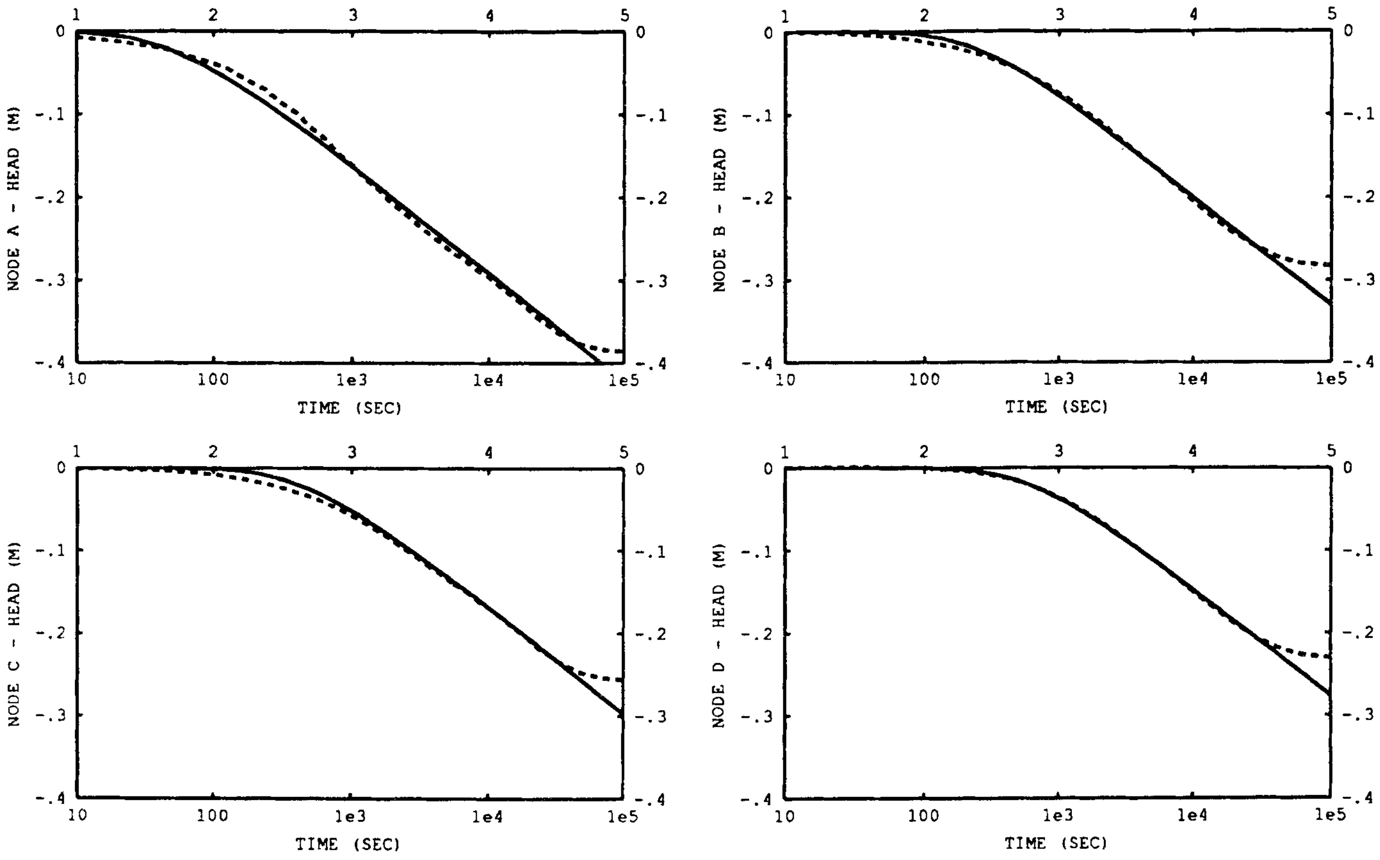

Figure 5. Comparison of analytic and LESFEM heads versus time. Solid lines are the Theis solution and dashed lines are the LESFEM-computed heads. Node locations can be found in Figure 1

Steady state fluxes can be computed from the analytical infinite aquifer solution of Thiem.[12] Two LESFEM x-direction flux profiles are compared with the flux profiles derived from the Thiem solution in Figure 6. The first profile starts at the pumping well and strikes directly west, while the second starts at the pumping well and strikes southwest at 225°. The west–east profile matches the analytical solution quite well except in the source element, where, as discussed earlier, it must change signs and consequently pass through zero. The effect of adding the singular solution to produce better tracking velocities in the source element is also shown in Figure 6. In the southwest–northeast profile the singular solution does not start until the profile has crossed

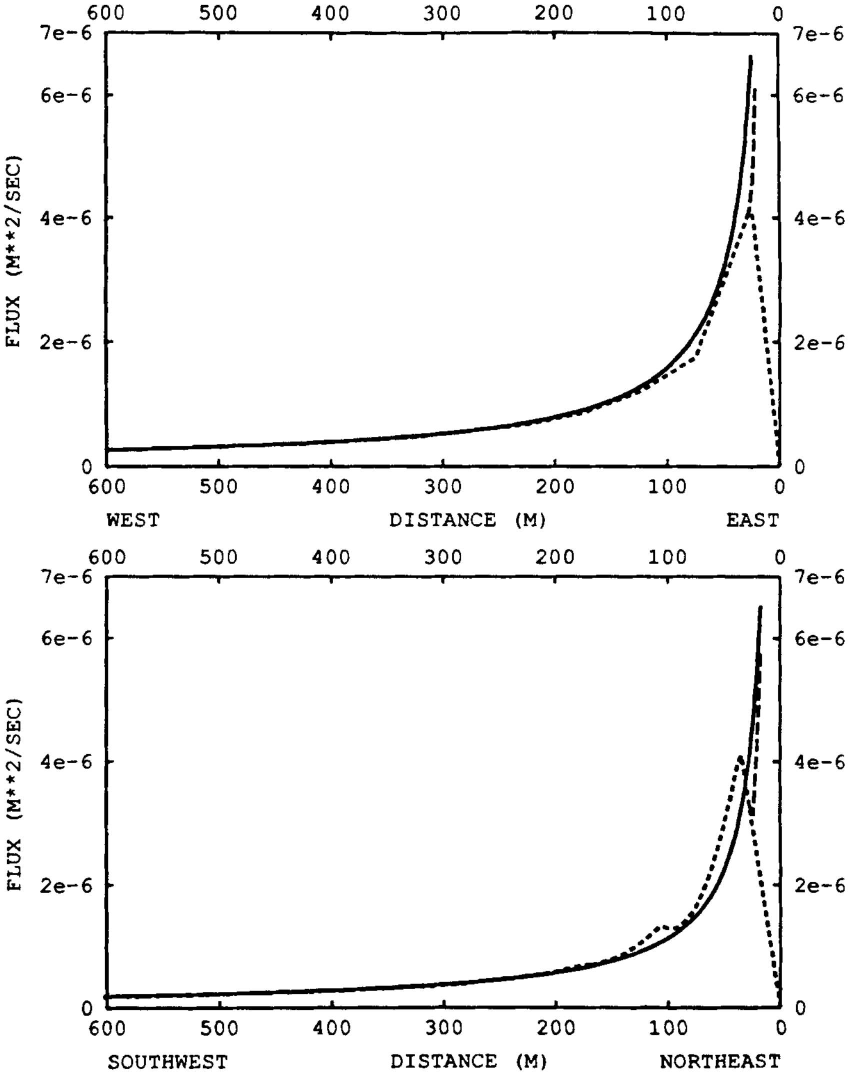

Figure 6. Comparison of analytic and LESFEM steady state flux profiles. The x-directed flux is profiled starting at the source location and striking 180° (top) and 225° (bottom). The solid line is the analytical solution, the short-dashed line is the LESFEM solution and the long-dashed line shows the effect of adding the singular trial function to the LESFEM solution

a portion of the source element and a small tracking velocity abnormality will be located just inside the element boundary.

At steady state the total flux into the domain must equal the total flux out of the domain and the total flux out of the domain should be

$$\int_{\delta\Omega} \mathbf{q}\cdot\mathbf{n}\,\mathrm{d}(\delta\Omega)=Q_p, \tag{19}$$

where $\mathbf{n}$ is the outward-directed normal vector and $\mathbf{q}$ is the flux vector. The LESFEM flux out of the domain, as computed by a contour integral around the domain boundary, differs from the pumping well source by less than 0·1%.

For comparison, the steady state problem was also solved by the Galerkin finite element method (FEM). A quadrant of the circular aquifer was discretized using the bilinear, quadrilateral finite element mesh shown in Figure 7. The LESFEM mesh has three unknowns associated with each node. Consequently the FEM mesh is refined relative to the LESFEM mesh so that the total number of unknowns per unit area is approximately the same for two discretizations. The source is located in the exact centre of the aquifer or at the northeast corner of the mesh. Owing to the symmetry of the problem, the northern and eastern straightline segments of the boundaries of the FEM mesh were modelled as no-flow boundaries. The curved segment of the boundary was once again modelled as a constant head of zero.

The FEM x-directed flux profiles starting at the source and striking west and starting at the source and striking southwest are shown in Figure 8. The east–west profile has a distinct step-like structure, because the x-directed flux values are constant across the elements in this direction. The northeast–southwest profile has a very large velocity error as the first element boundary is approached. The LESFEM results shown in Figure 6 are smoother and the magnitude of the largest point errors are smaller than the magnitude of the largest FEM point errors. The FEM

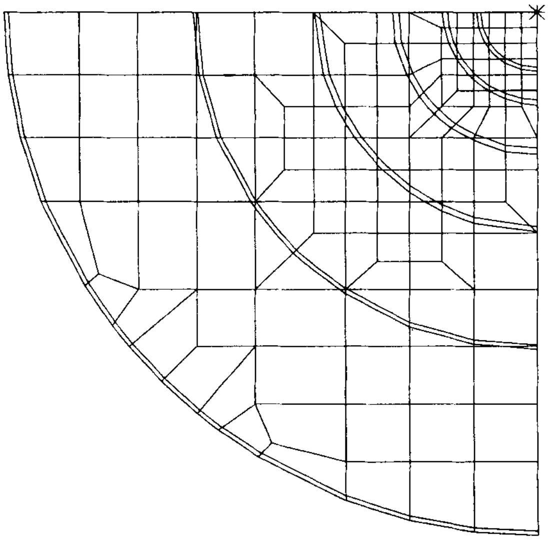

Figure 7. Galerkin finite element mesh. One quadrant of a circular aquifer with radius 1000 m is discretized using quadrilateral finite elements. Pumping well source is indicated with a star. Steady state hydraulic heads as computed by the Galerkin method are contoured with double lines at the interval of 0·05 m, with the zero contour falling on the curved segment of the boundary

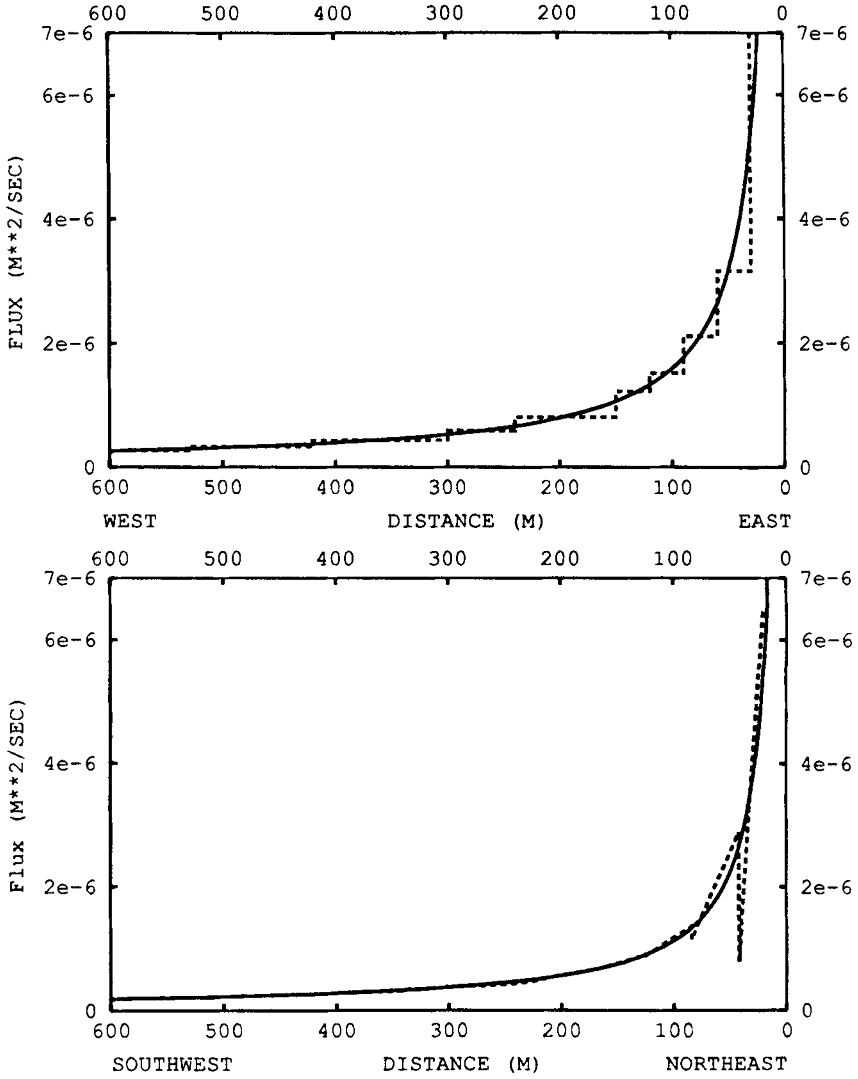

Figure 8. Comparison of analytic and FEM steady state flux profiles. The x-directed flux is profiled starting at the source location and striking 180° (top) and 225° (bottom). The solid line is the analytical solution and the short-dashed line is the FEM solution

y-directed flux profiles along the same two profiles are shown in Figure 9. Since the east–west profile is along a streamline which has been modelled as a no-flow boundary, the y-directed flux should be zero. From Figure 9 it is evident that serious y-directed flux errors occur near the source location. In contrast, the LESFEM y-directed fluxes along this profile are of the order of 10^{-9} or less. The y-directed flux of the FEM solution shown in Figure 9 has some abnormalities in the area of 200–350 m. These abnormalities arise from non-rectangular isoparametric elements which are located along the profile.

In summary, despite some irregularities, the LESFEM algorithm has performed well. The grid has been successfully refined, the transient behaviour of the head solution has been captured and

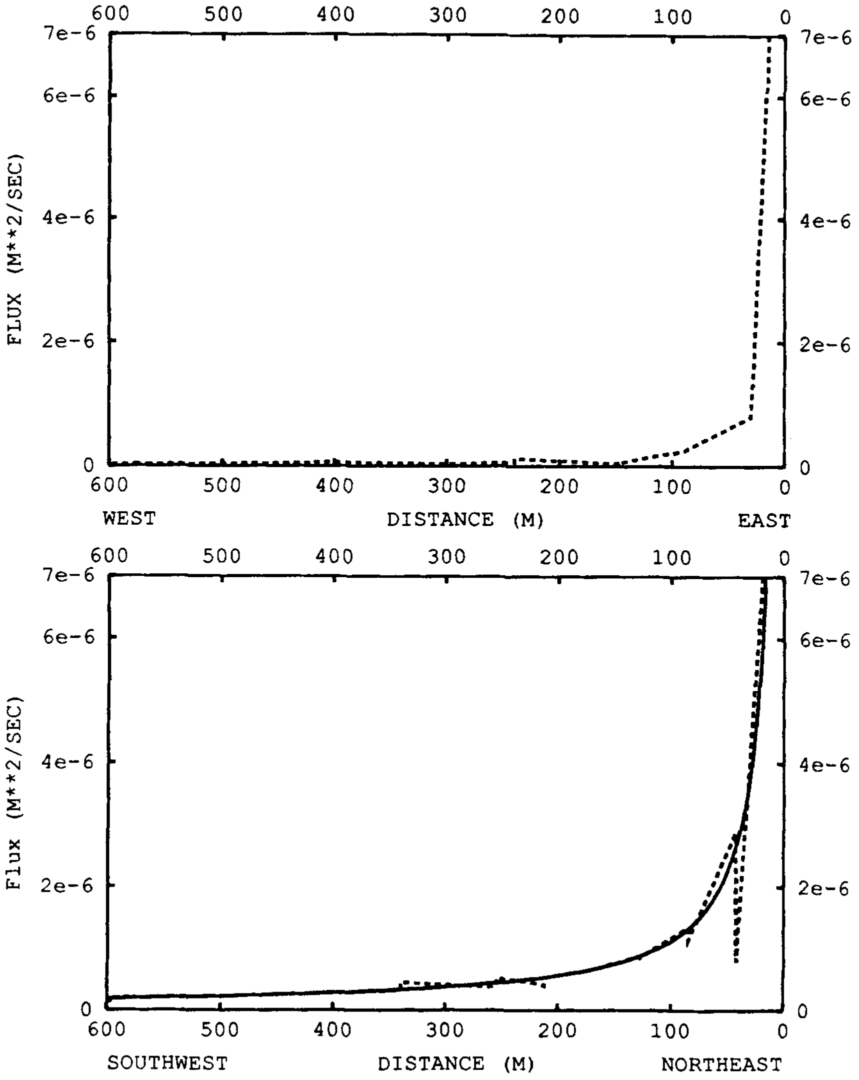

Figure 9. Comparison of analytic and FEM steady state flux profiles. The y-directed flux is profiled starting at the source location and striking 180° (top) and 225° (bottom). The solid line is the analytical solution and the short-dashed line is the FEM solution. The analytic y-directed flux in the east–west profile is zero

the circular geometry of the boundary has been reproduced. Irregularities in the fluxes are observed near the point source but they rapidly diminish away from the source. In contrast, the FEM mesh is more difficult to construct and the FEM results have some very large errors that can cause tracking problems. Note that even with the mixed formulation the flux solutions are more susceptible to abnormalities than the head solutions.

RAIN ON THE PLANE

In the following example the LESFEM flow algorithm is used to compute the steady state solution to uniform infiltration into a phreatic aquifer. The finite element grid and aquifer

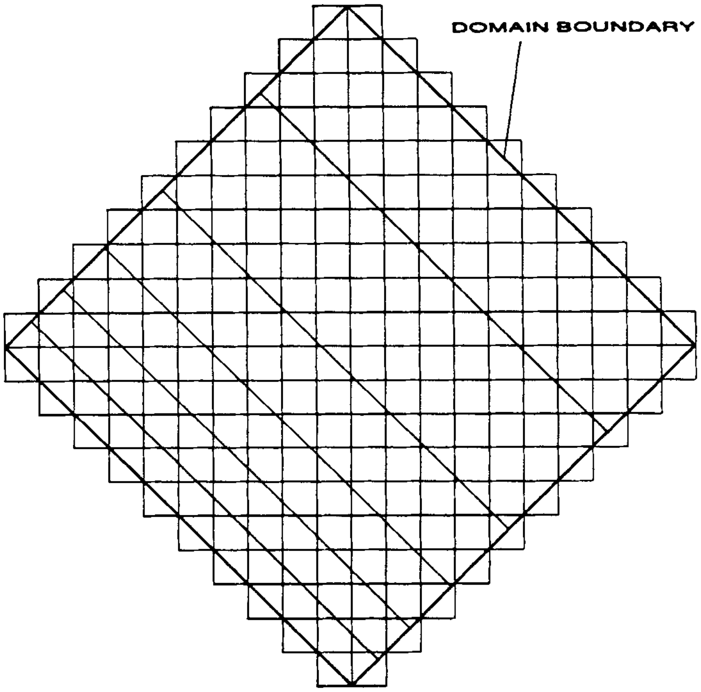

Figure 10. LESFEM mesh—rain on the plane. A square domain, rotated 45° relative to the grid orientation, is inscribed on the orthogonal mesh. Element dimensions are 100 m × 100 m. Heads are contoured at 0·5 m intervals, starting at the 3 m contour which overlies the constant-head boundary at the lower left

boundaries are illustrated in Figure 10. The grid element dimensions are 100 m × 100 m. A square domain is inscribed on the orthogonal mesh. The aquifer boundaries and the resulting flow direction are rotated 45° relative to the grid orientation.

The hypothetical aquifer has an impermeable bottom at elevation $b=0$. The aquifer is homogeneous, isotropic and has hydraulic conductivity $K_{xx}=K_{yy}=1{\cdot}4\times10^{-4}\,\mathrm{m\,s^{-1}}$. It is bounded on the southwest by a fully connected stream and the boundary is modelled as having a constant head of 3 m. The northeast boundary is a groundwater divide and a no-flow boundary condition is applied. The northwest and southeast boundaries follow streamlines and are consequently modelled as no-flow boundaries. The areal dimension of the aquifer is approximately 1414 m × 1414 m. The entire aquifer is subject to a uniform infiltration rate of $I=1{\cdot}61\times10^{-9}\,\mathrm{m\,s^{-1}}$ (2 in year^{-1}). Since the aquifer is not aligned with the grid, the problem is two-dimensional. However, in the direction of flow the problem reduces to one dimension and can be solved analytically.

A potential scale of $P=2{\cdot}3\times10^5$ was used along with boundary weights $Wb_{1,l_1}=10^4$ and $Wb_{2,l_2}=10^4$. The Darcy's law residual weights were computed using equations (18b) and (18c). When the conservation-of-mass residuals were computed using the weights of equation (18a), the boundary integral of the LESFEM flux out of the domain was in error by 3%. Consequently, conservation-of-mass weights were increased by a factor of two and flux errors were reduced to less than 1%. The free surface convergence criterion was $\varepsilon_h=0{\cdot}01$ m. Starting with a constant head of 3 m and zero flux, the algorithm converged after five free surface iterations.

Head values of the numerical solution are contoured in Figure 10. The 3 m contour coincides with the southeastern constant-head boundary. Other contours are straight lines which are

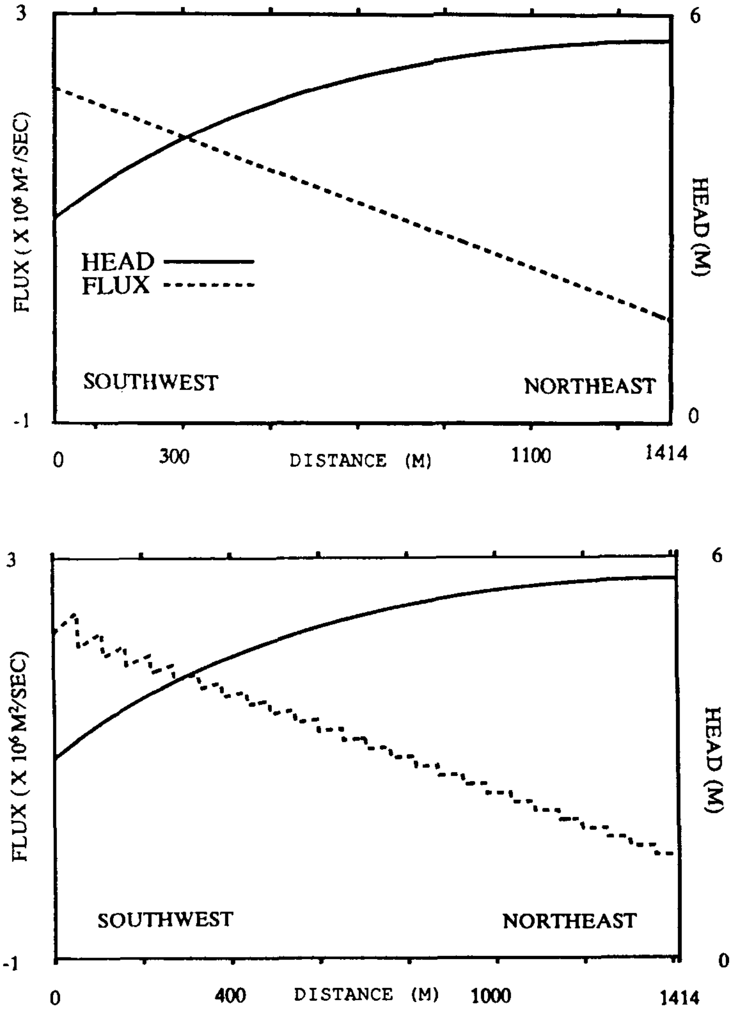

Figure 11. Head and total flux profiles. In the upper figure, LESFEM-computed heads (solid line) and total flux values (broken line) are profiled along the centreline of the domain shown in Figure 10. In the lower figure, FEM-computed heads (solid line) and total flux values (broken line) are profiled along the centreline of an equivalent mesh made of square elements aligned with the aquifer boundaries

perpendicular to the direction of flow. The maximum value of the computed head, 5·65 m, is found at the northeast boundary. Figure 11 presents a southwest–northeast profile of the head and absolute value of the flux along the centreline of the aquifer. The head values have the parabolic shape predicted by the analytical solution. The maximum difference at a node between the computed head and the analytical head is 0·011 m. Figure 11 also shows that the computed solution has captured the linear decrease in flux with increasing distance from the river predicted by the analytical solution.

The same problem was solved with the FEM algorithm. A square grid of 27 nodes by 27 nodes was superimposed on the aquifer so that the x-direction was aligned with the flow. As with the previous example, the number of degrees of freedom used for the FEM calculation and the LESFEM calculation were approximately equal. The FEM-computed head profile and flux profile are shown in the lower part of Figure 11. The FEM solution has captured the parabolic shape of the head solution. In contrast to the accurate head solution, the flux profile demonstrates a sawtoothed shape, because the derivative of the head is constant across the elements and the transmissivity changes with the change in the free surface elevation. The LESFEM and FEM flux profiles shown in Figure 11 demonstrate the advantages of the mixed finite element procedure.

The maximum difference at a node between the LESFEM-computed and analytical x- or y-direction fluxes is $1{\cdot}3 \times 10^{-8}$ m^2 s^{-1}. The percentage error is defined as the absolute value of the difference between the computed and analytical values divided by the analytical value. The percentage error in flux averaged over all the nodes is 0·5%. Replacing Q_p in equation (19) with I times the area of the domain, the percentage error in global flux was found to be 0·8%. Finally, Figure 12 shows the flux vectors of the computed solution. The flux vectors are parallel to the streamline boundaries and increase in magnitude as they approach the discharge boundary.

The LESFEM algorithm has produced an accurate solution to the steady state non-linear free surface problem. The shape of the free surface has been captured to within the accuracy of the convergence criterion. Although the grid boundaries are not aligned with the grid, the boundary conditions have been effectively imposed. The algorithm has produced accurate flux values with the point errors generally less than 1%. The global flux balance is also good. Errors in the flux arising from the differentiation of the head that is required by the standard FEM method have been eliminated.

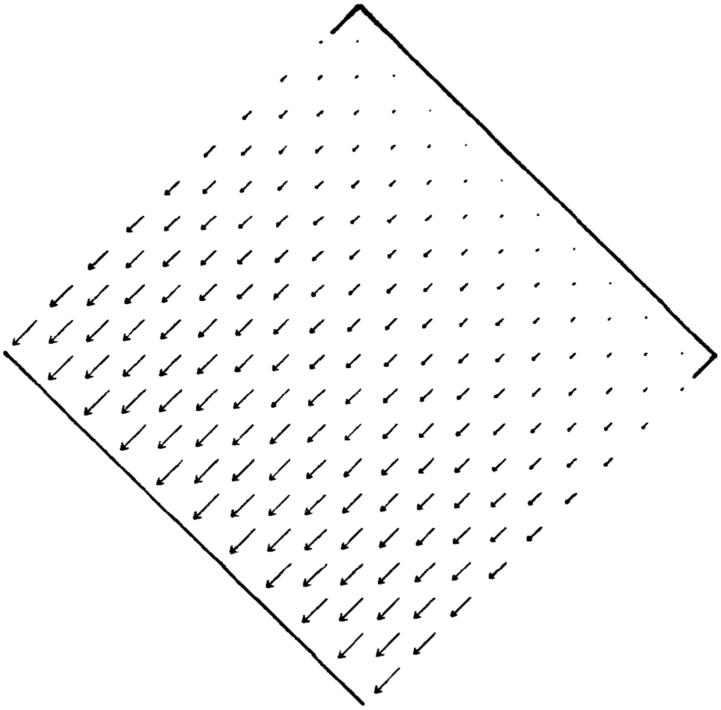

Figure 12. LESFEM flux vectors. LESFEM flux vectors are plotted on the rotated domain of Figure 10. The northwest–southeast-trending domain boundaries are shown as solid lines. The outer lines of flux vectors fall on the southwest–northeast-trending no-flow boundaries

CONCLUSIONS

A least-squares mixed finite element groundwater flow algorithm (LESFEM) has been introduced. Hydraulic head and x- and y-direction fluxes are used as state variables. Residuals are written for conservation of mass, Darcy's law and boundary conditions. The residuals are evaluated at collocation points, weighted, squared, summed and minimized by taking the derivatives with respect to the degrees of freedom in the approximation for the state variables and setting them to zero. Wells are incorporated into source elements, and velocity singularities are accurately handled by not applying Darcy's law within the source element. For tracking purposes, velocities within the source element are interpolated using a singular velocity function. Both flux and velocity are C^0 continuous.

Test problem results demonstrate the accommodation of irregular boundaries on an orthogonal mesh and a grid refinement technique which uses orthogonal elements and hanging nodes. It has also been demonstrated that accurate velocity and head values can be produced for transient, steady state and free surface problems.

When accurate fluxes are the main objective of a simulation, the mixed finite element formulation is superior to the classical formulation, because head values do not need to be differentiated in order to produce fluxes. Pathologies in the computed head are not amplified in the flux. Similarly, the order of the flux approximation is the same as the order of the head approximation. However, fluxes are still more prone to abnormalities than are the heads.

Although guidelines for weighting and scaling have been presented, care must be taken that the conservation of mass is sufficiently enforced. A global flux conservation calculation should be done for steady state solutions to assure that the forcing from the conservation-of-mass equations is sufficiently represented. If not, the conservation-of-mass residual weight should be increased by a factor of two to three. Using the proposed scaling and weighting schemes, experimental convergence rates of order one for the maximum point error were obtained for both head and flux. Experimental convergence rates approaching order two were obtained for the L_2-error norm for both head and flux.

Irregular domains and local grid refinement are constructed on orthogonal meshes. Use of orthogonal meshes allows simple, automated mesh generation procedures. Similarly, combining the penalty method for enforcing boundary conditions with an orthogonal mesh allows simple, automated boundary specification. Finally, tracking is simplified on an orthogonal mesh.

ACKNOWLEDGEMENTS

We wish to acknowledge support of the Air Force Office of Scientific Research, Bolling AFB, DC and support from Department of Energy Grant DEFG02-86ER60453.

APPENDIX: MATRIX STRUCTURE

The discrete set of equations (17) can be written in matrix form as

$$\mathbf{AX}=\mathbf{B}. \tag{20}$$

The elements of the unknown vector $\mathbf{X}$ are related to the state variables by

$$x_{3(I-1)+1}=H_I', \quad I=1,\ldots,M, \tag{21a}$$

$$x_{3(I-1)+2}=QX_I, \quad I=1,\ldots,M, \tag{21b}$$

$$x_{3(I-1)+3}=QY_I, \quad I=1,\ldots,M, \tag{21c}$$

where I is a node index. The global unknown indices are divided into three subsets such that I_1', I_2', and I_3' are the unknown indices found in equations (21a)–(21c) respectively.

The elements of the system matrix **A** are

$$\begin{aligned}a_{I_1'J_1'} = \sum_{k=1}^{NK} \Bigg[& Wm_k^2 P\left(\frac{S^k}{\Delta t}+B^k\right)\psi_{J_1'}^k P\left(\frac{S^k}{\Delta t}+B^k\right)\psi_{I_1'}^k \\ & + Wq_{x,k}^2\left(\frac{2PT_{xx}^k}{\Delta x^e}\frac{\partial\psi_{J_1'}^k}{\partial\xi}+\frac{2PT_{xy}^k}{\Delta y^e}\frac{\partial\psi_{J_1'}^k}{\partial\eta}\right)\left(\frac{2PT_{xx}^k}{\Delta x^e}\frac{\partial\psi_{I_1'}^k}{\partial\xi}+\frac{2PT_{xy}^k}{\Delta y^e}\frac{\partial\psi_{I_1'}^k}{\partial\eta}\right) \\ & + Wq_{y,k}^2\left(\frac{2PT_{xy}^k}{\Delta x^e}\frac{\partial\psi_{J_1'}^k}{\partial\xi}+\frac{2PT_{yy}^k}{\Delta y^e}\frac{\partial\psi_{J_1'}^k}{\partial\eta}\right)\left(\frac{2PT_{xy}^k}{\Delta x^e}\frac{\partial\psi_{I_1'}^k}{\partial\xi}+\frac{2PT_{yy}^k}{\Delta y^e}\frac{\partial\psi_{I_1'}^k}{\partial\eta}\right)\Bigg] \\ & + \sum_{l_1=1}^{NB_1} Wb_{1,l_1}^2\psi_{J_1'}^{l_1}\psi_{I_1'}^{l_1} + \sum_{l_3=1}^{NB_3} Wb_{3,l_3}^2 PB_{\mathrm{b}}^{l_3}\psi_{J_1'}^{l_3} PB_{\mathrm{b}}^{l_3}\psi_{I_1'}^{l_3},\end{aligned}\tag{22}$$

$$\begin{aligned}a_{I_1'J_2'} = \sum_{k=1}^{NK} \Bigg[& Wm_k^2\frac{\partial\psi_{J_2'}^k}{\partial\xi}\frac{2P}{\Delta x^e}\left(\frac{S^k}{\Delta t}+B^k\right)\psi_{I_1'}^k + Wq_{x,k}^2\psi_{J_2'}^k\left(\frac{2PT_{xx}^k}{\Delta x^e}\frac{\partial\psi_{I_1'}^k}{\partial\xi}+\frac{2PT_{xy}^k}{\Delta y^e}\frac{\partial\psi_{I_1'}^k}{\partial\eta}\right)\Bigg] \\ & - \sum_{l_3=1}^{NB_3} Wb_{3,l_3}^2\psi_{J_2'}^{l_3}\cos\nu^{l_3} PB_{\mathrm{b}}^{l_3}\psi_{I_1'}^{l_3},\end{aligned}\tag{22b}$$

$$\begin{aligned}a_{I_1'J_3'} = \sum_{k=1}^{NK} \Bigg[& Wm_k^2\frac{\partial\psi_{J_3'}^k}{\partial\eta}\frac{2P}{\Delta y^e}\left(\frac{S^k}{\Delta t}+B^k\right)\psi_{I_1'}^k + Wq_{y,k}^2\psi_{J_3'}^k\left(\frac{2PT_{xy}^k}{\Delta x^e}\frac{\partial\psi_{I_1'}^k}{\partial\xi}+\frac{2PT_{yy}^k}{\Delta y^e}\frac{\partial\psi_{I_1'}^k}{\partial\eta}\right)\Bigg] \\ & - \sum_{l_3=1}^{NB_3} Wb_{3,l_3}^2\psi_{J_3'}^{l_3}\sin\nu^{l_3} PB_{\mathrm{b}}^{l_3}\psi_{I_1'}^{l_3},\end{aligned}\tag{22c}$$

$$\begin{aligned}a_{I_2'J_2'} = \sum_{k=1}^{NK} & Wm_k^2\left(\frac{2}{\Delta x^e}\frac{\partial\psi_{J_2'}^k}{\partial\xi}\frac{2}{\Delta x^e}\frac{\partial\psi_{I_2'}^k}{\partial\xi}+Wq_{x,k}^2\psi_{J_2'}^k\psi_{I_2'}^k\right) \\ & + \sum_{l_2=1}^{NB_2} Wb_{2,l_2}^2\psi_{J_2'}^{l_2}\cos\nu^{l_2}\psi_{I_2'}^{l_2}\cos\nu^{l_2} + \sum_{l_3=1}^{NB_3} Wb_{3,l_3}^2\psi_{J_2'}^{l_3}\cos\nu^{l_3}\psi_{I_2'}^{l_3}\cos\nu^{l_3},\end{aligned}\tag{22d}$$

$$\begin{aligned}a_{I_2'J_3'} = \sum_{k=1}^{NK} & Wm_k^2\frac{2}{\Delta y^e}\frac{\partial\psi_{J_3'}^k}{\partial\eta}\frac{2}{\Delta x^e}\frac{\partial\psi_{I_2'}^k}{\partial\xi} \\ & + \sum_{l_2=1}^{NB_2} Wb_{2,l_2}^2\psi_{J_3'}^{l_2}\sin\nu^{l_2}\psi_{I_2'}^{l_2}\cos\nu^{l_2} + \sum_{l_3=1}^{NB_3} Wb_{3,l_3}^2\psi_{J_3'}^{l_3}\sin\nu^{l_3}\psi_{I_2'}^{l_3}\cos\nu^{l_3},\end{aligned}\tag{22e}$$

$$\begin{aligned}a_{I_3'J_3'} = \sum_{k=1}^{NK} & \left(Wm_k^2\frac{2}{\Delta y^e}\frac{\partial\psi_{J_3'}^k}{\partial\eta}\frac{2}{\Delta y^e}\frac{\partial\psi_{I_3'}^k}{\partial\eta}+Wq_{y,k}^2\psi_{J_3'}^k\psi_{I_3'}^k\right) \\ & + \sum_{l_2=1}^{NB_2} Wb_{2,l_2}^2\psi_{J_3'}^{l_2}\sin\nu^{l_2}\psi_{I_3'}^{l_2}\sin\nu^{l_2} + \sum_{l_3=1}^{NB_3} Wb_{3,l_3}^2\psi_{J_3'}^{l_3}\sin\nu^{l_3}\psi_{I_3'}^{l_3}\sin\nu^{l_3},\end{aligned}\tag{22f}$$

$$a_{I_2'J_1'} = a_{I_1'J_2'},\tag{22g}$$

$$a_{I_3'J_1'} = a_{I_1'J_3'},\tag{22h}$$

$$a_{I_3'J_2'} = a_{I_2'J_3'}.\tag{22i}$$

The three sets of the load vector elements are

$$\begin{aligned} b_{I'_1} = {} & \sum_{k=1}^{NK} Wm_k^2 \left(\frac{PS^k}{\Delta t} \hat{h}_k^{n-1} + B^k h_{\mathrm{r}}^k + I^k \right) P \left(\frac{S^k}{\Delta t} + B^k \right) \psi_{I'_1}^k \\ & + \sum_{l_1=1}^{NB_1} Wb_{1,l_1}^2 \frac{b_1^{l_1}}{P} \psi_{I'_1}^{l_1} + \sum_{l_3=1}^{NB_3} Wb_{3,l_3}^2 B_{\mathrm{b}}^{l_3} h_{\mathrm{br}}^{l_3} P B_{\mathrm{b}}^{l_3} \psi_{I'_3}^{l_3}, \end{aligned} \tag{23a}$$

$$\begin{aligned} b_{I'_2} = {} & \sum_{k=1}^{NK} Wm_k^2 \left(\frac{PS^k}{\Delta t} \hat{h}_k^{n-1} + B^k h_{\mathrm{r}}^k + I^k \right) \frac{2}{\Delta x^e} \frac{\partial \psi_{I'_2}^k}{\partial \xi} \\ & + \sum_{l_2=1}^{NB_2} Wb_{2,l_2}^2 b_2^{l_2} \psi_{I'_2}^{l_2} \cos v^{l_2} - \sum_{l_3=1}^{NB_3} Wb_{3,l_3}^2 B_{\mathrm{b}}^{l_3} h_{\mathrm{br}}^{l_3} \psi_{I'_2}^{l_3} \cos v^{l_3}, \end{aligned} \tag{23b}$$

$$\begin{aligned} b_{I'_3} = {} & \sum_{k=1}^{NK} Wm_k^2 \left(\frac{PS^k}{\Delta t} \hat{h}_k^{n-1} + B^k h_{\mathrm{r}}^k + I^k \right) \frac{2}{\Delta y^e} \frac{\partial \psi_{I'_3}^k}{\partial \eta} \\ & + \sum_{l_2=1}^{NB_2} Wb_{2,l_2}^2 b_2^{l_2} \psi_{I'_3}^{l_2} \sin v^{l_2} - \sum_{l_3=1}^{NB_3} Wb_{3,l_3}^2 B_{\mathrm{b}}^{l_3} h_{\mathrm{br}}^{l_3} \psi_{I'_3}^{l_3} \sin v^{l_3}, \end{aligned} \tag{23c}$$

where the point source terms are now included in the areal flux term I^k.

REFERENCES

1. D. E. Eason, 'A review of least-squares methods for solving partial differential equations', *Int. j. numer. methods eng.*, **10**, 1021–1046 (1976).
2. P. J. Harley and A. R. Mitchell, 'A finite element collocation method for the exact control of a parabolic problem', *Int. j. numer. methods eng.*, **11**, 345–353 (1977).
3. W. L. Kwok and Y. K. Cheung, 'Application of least square collocation technique in finite element and finite strip formulation', *Int. j. numer. methods eng.*, **11**, 1391–1404 (1977).
4. B. Joos, 'The least squares collocation method for solving partial differential equations', *Ph.D. Dissertation*, Princeton University, 1986.
5. J. P. Laible and G. F. Pinder, 'Least squares collocation of differential equations on irregularly shaped domains using orthogonal meshes', *Numer. Methods Partial Differ. Eqns.*, **5**, 347–361 (1989).
6. P. P. Lynn and S. K. Arya, 'Use of the least squares criterion in the finite element formulation', *Int. j. numer. methods eng.*, **6**, 75–88 (1973).
7. P. P. Lynn and S. K. Arya, 'Finite elements formulated by the weighted discrete least squares method', *Int. j. numer. methods eng.*, **8**, 71–90 (1974).
8. A. K. Aziz, R. B. Kellog and A. B. Stephens, 'Least squares methods for elliptic systems', *Math. Comput.*, **44**, 53–70 (1985).
9. R. E. Ewing and J. V. Koebbe, 'Mixed finite element methods for groundwater flow and contaminant transport', in R. Vichnevetsky and R. S. Stepeleman (eds), *Proc. Fifth IMACS Int. Symp. on Computer Methods for Partial Differential Equations*, Bethlehem, Pennsylvania. IMACS, New Brunswick, New Jersey, 1984, pp. 106–113.
10. M. B. Allen, R. E. Ewing and J. V. Koebbe, 'Mixed finite element methods for computing groundwater velocities', *Numer. Methods Partial Differ. Eqns.*, **3**, 195–207 (1985).
11. P. S. Huyakorn and G. F. Pinder, *Computational Methods in Subsurface flow*, Academic, New York, 1983.
12. G. P. Kruseman and N. A. DeRidder, 'Analysis and evaluation of pumping test data', *Bulleting 11 16R1*, International Institute for Land Reclamation and Improvement/ILRI, Wageningen, The Netherlands, 1983, p. 200.